ibe
Advancing Biology-Inspired Engineering
Official publication of the Institute of Biological Engineering

Seaweed-based alginate/hydroxyapatite composite for the effective removal of bacteria, cyanobacteria, algae, and crystal violet from water

Mohamed Gomaa[1]* and Amal William Danial[1]

Abstract

A novel cost-effective and multifunctional nanocomposite was developed based on sustainable macroalgae bio-mass. The brown seaweed *Sargassum latifolium* was utilized for alginate extraction and the calcareous red seaweed *Tricleocarpa fragilis* was utilized as $CaCO_3$ source for nanohydroxyapatite synthesis. The developed Zn^{2+}-crosslinked alginate/nanohydroxyapatite (ZA/nHA) beads were characterized by FT-IR, XRD, and TEM. The antimicrobial potential of ZA/nHA to disinfect synthetic *Escherichia coli*-contaminated water was evaluated at different bacterial load and composite concentrations. The developed ZA/nHA effectively inactivated bacteria at initial concentration $\leq 10^5$ CFU mL^{-1} and 0.5–1% (w/v) of ZA/nHA within 300–360 min. The kinetics of bacterial disinfection exhibited better fitting to Weibull model than Log-liner model, which confirmed the disinfection process. Furthermore, treatment of the cyanobacterium (*Chroococcus* sp.) and the microalga (*Chlorella* sp.) with ZA/nHA showed promising antialgal properties as indicated by reductions in chlorophyll a. The treatment indicated 100% and 90% removal of *Chroococcus* sp. and *Chlorella* sp. within 2 and 4 days, respectively. The developed ZA/nHA also exhibited a promising application as a biosorbent for crystal violet (CV). The adsorption process was very fast (0.171 mg CV g^{-1} adsorbent was removed within 7 min at pH 6.0). The adsorption kinetics exhibited better fitting to the pseudo-second order and Elovich mod-els than the pseudo-first order equation. Besides, Sips model better represented the isotherm data of CV adsorption. The thermodynamic analysis indicated exothermic adsorption, which became more favorable at low temperature and high CV concentration. The developed nanocomposite is eco-friendly and suitable for multiple environmental applications.

Keywords *E. coli*, Disinfection, Antialgal, Biosorption, Nanocomposite, nanohydroxyapatite
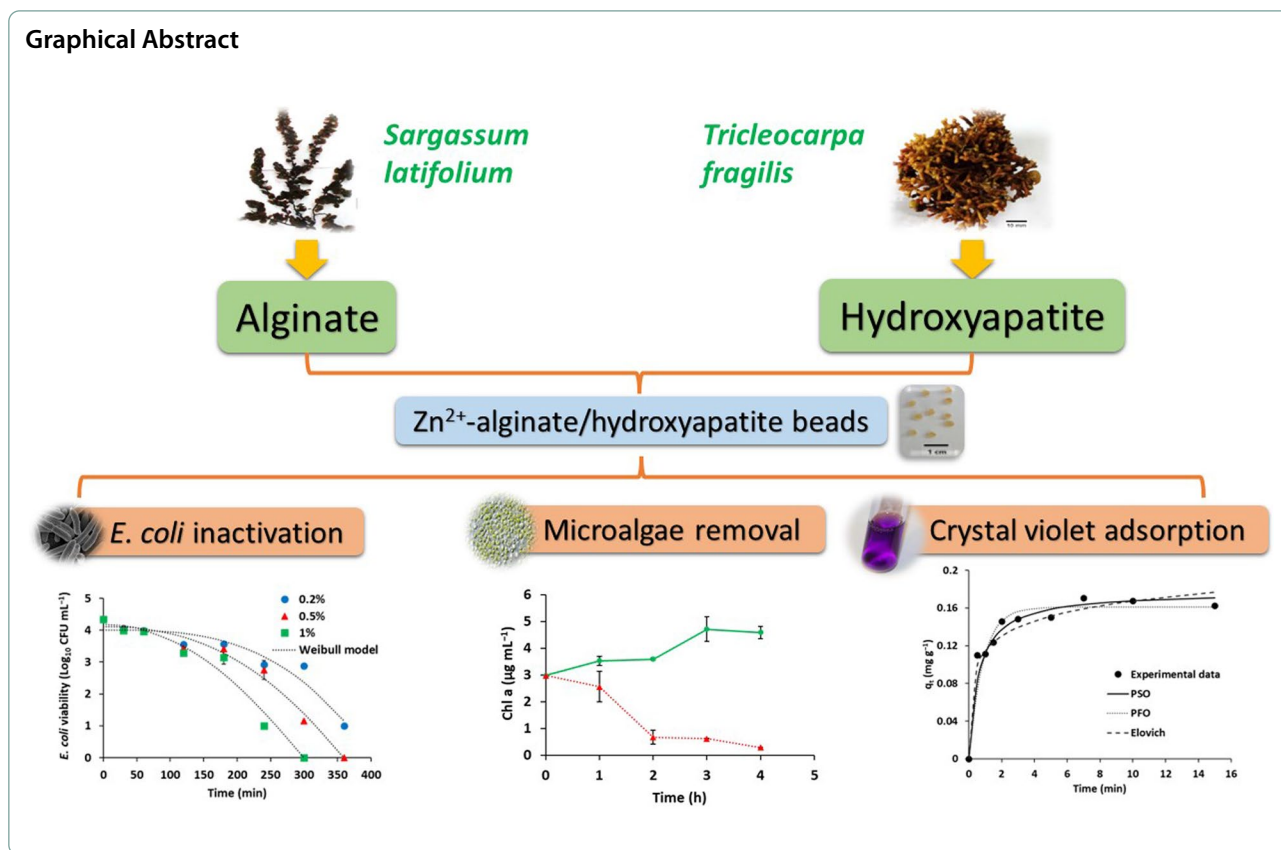
*Correspondence:
Mohamed Gomaa
m_gomaa@aun.edu.eg
Full list of author information is available at the end of the article

Graphical Abstract

Introduction

Accessing clean, safe, and sustainable resources of water as well as the removal of hazardous contaminants from polluted water resources are one of the main demands of the current century. Microbial contamination of drinking water generally threatens human life by transmitting serious diseases such as diarrhea and dysentery [1]. The total number of coliforms and *Escherichia coli* in drinking water must be zero according to the guidelines of the Environmental Protection Agency [2] and the World Health Organization [1]. On the other hand, the increase of nutrients in the aquatic environment results in the development of harmful cyanobacterial and algal blooms, which also represent an enormous danger to human health and the whole ecosystem [3]. Similarly, aquatic pollution by persistent and toxic dyes from various industries can cause severe damage to ecosystem and life-threatening diseases after accumulation in human body [4]. Cystal violet (CV) is a common cationic dye in textile industry as well as in the preparation of paints and printing ink [5]. CV is also utilized as a biological stain, a skin disinfectant, and a bacteriostatic agent in the medical community and veterinary medicine. Besides, it is usually incorporated into poultry feed to prevent the growth of pathogenic microorganisms [6]. Despite its extensive applications, CV is carcinogenic and generally regarded as recalcitrant compound since it is non-biodegradable and can persist in different environments [5, 6].

In general, the common practices for the disinfection of water supplies include chemical methods (chlorine, ozone, iodine) and physical methods (UV radiation) [7]. Although these techniques are effective in eliminating undesired microbes, they can induce the formation of harmful byproducts that are carcinogenic [8]. Furthermore, the traditional practices for the treatment of dye-bearing wastewater include adsorption, membrane filtration, coagulation, ozonation, electrolysis, and photocatalysis as well as biodegradation using microorganisms and enzymes [9]. Among these technique, adsorption-based processes have been identified as a promising technology owing to their comparatively low operation costs, simplicity, and effectivity [10, 11].

Marine macroalgae are valuable and sustainable resources for the production of cost-effective materials for various applications. The seaweed biomass of Phaeophyceae (brown algae) contains important structural polysaccharides such as alginates. Alginate is the salt of alginic acid, which is a linear anionic hetero-polysaccharide consisting of D-mannuronic acid (M) and L-guluronic acid (G) [12]. The M and G residues occur in

varying relative proportions and are organized in different blocks as MM, MG, and GG within the same chain of alginate [13]. Alginates are generally characterized by the ability to cross-link divalent cations such as Ca^{2+} and Zn^{2+}, resulting in the formation of insoluble hydrogels with 3-D structures. Generally, alginates are exploited in different industries and biotechnological applications as thickeners, chelators, encapsulators and gel-forming agents [12].

On the other hand, some members of the Rhodophyceae (Red algae) are calcareous, which contain $CaCO_3$ as a structural component in their skeleton. Although calcified macroalgae are widely distributed all over the world, their $CaCO_3$ skeletons are less explored due to poor stability [14]. One route for the effective utilization of calcified biomass in biotechnology may rely on the conversion of hard $CaCO_3$ skeletons into more stable material such as hydroxyapatite. Hydroxyapatite (HA) $(Ca_{10}(PO_4)6(OH)_2)$ is a promising bioactive ceramic material which is similar in composition and mechanical strength to the hard tissues of the human body [15]. However, little information is available in the literature regarding the utilization of calcified marine macroalgae for the preparation of nanohydroxyapatite. One study synthesized hydroxyapatite nanocrystals from mineralized *Corallina officinallis*, red alga, by thermal and chemical route [14]. However, no attempts have been carried out to develop nanohydroxyapatite from calcified red algae using chemical treatment only. The use of hydroxyapatite is generally limited by its brittleness and regeneration, which is avoided by formation of polymer/hydroxyapatite composite [16]. For instance, alginate/nanohydroxyapatite composites have gained a growing attention to combine the unique features of these compounds and produce hybrid materials with important characteristics such as biodegradability, non-toxicity, biocompatibility, etc. [17, 18]. Alginate/nanohydroxyapatite have been utilized as an eco-friendly composite for the adsorptive removal of methylene blue [16], lead [17], and fluoride [18]. Furthermore, this hybrid material exhibited excellent antibacterial properties against food-borne pathogens [19]. However, to the best of our knowledge, this is the first attempt of utilizing macroalgae waste as a cost-effective biomass for the preparation of Zn^{2+}-crosslinked alginate/nanohydroxyapatite composite. Furthermore, a novel method was employed for obtaining nanohydroxyapatite from calcified macroalgae based on direct chemical precipitation.

The aim of the current study was to utilize the sustainable biomass of macroalgae for cost effective preparation of Zn^{2+}-crosslinked alginate/nanohydroxyapatite composite beads. The developed nanocomposite was evaluated for mutable purposes including the disinfection of *E. coli*-contaminated water and removal of cyanobacteria (*Chroococcus* sp.) and microalgae (*Chlorella* sp.). Furthermore, the nanocomposite was evaluated as a biosorbent for the removal of crystal violet from aqueous solutions. The kinetics of *E.coli* disinfection as well as the kinetics, isotherms and thermodynamics of dye adsorption were also studied.

Materials and methods
### Macroalgal biomass
The brown seaweed *Sargassum latifolium* (Turner) C. Agardh and the red seaweed *Tricleocarpa fragilis* (Linnaeus) Huisman & R.A. Townsend were collected from the Red Sea coast, Egypt. The algal biomass was sun dried and pulverized using a home blender.

Extraction of alginate
The brown seaweed biomass was treated with a 3% w/v citric acid solution for 1 h at room temperature [11]. Acidic pretreatment removes fucoidan and the crosslinked cations with alginate and produces insoluble alginic acid within the seaweed biomass [11]. Then, the residual biomass was collected by filtration and subjected to alkaline treatment. The alkaline treatment involved the use of 2% w/v Na_2CO_3 at 40 °C for 2h. During this process the insoluble alginic acid is converted into soluble sodium alginate [11]. The extracted biomass is separated by filtration and sodium alginate in the filtrate was precipitated by double volume of ethanol. After 24 h at 4 °C, the precipitated sodium alginate (SA) was collected by filtration and oven dried (60 °C).

Preparation of hydroxyapatite
The calcified red alga (*T. fragilis*) was treated with 1 M HCl solution for 10 min to convert $CaCO_3$ in the cell wall into soluble $CaCl_2$ in the solution according to the following reaction:

$$2HCl + CaCO_3 \rightarrow CaCl_2 + CO_2 + H_2O$$
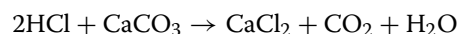
The $CaCl_2$ solution was collected by filtration and converted into calcium hydroxide according to the following reaction:

$$CaCl_2 + 2NaOH \rightarrow Ca(OH)_2 + 2NaCl$$
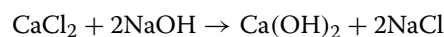
The precipitated calcium hydroxide was separated from the solution by centrifugation (3800 g, 10 min), oven dried and used for the synthesis of nanohydroxyapatite (nHA).

In a typical synthesis, 1 M of $Ca(OH)_2$ suspension is reacted with 0.6 M phosphoric acid under continuous stirring and the pH of the mixture is controlled by NH_4OH solution at pH 10 to avoid the formation of calcium deficient apatite [19]. The expected reaction is as follows.

$$10Ca(OH)_2 + 6H_3PO_4 \rightarrow +Ca_{10}(PO_4)_6(OH)_2 (Hydroxyapatite) + 18H_2O$$

The precipitated hydroxyapatite was separated by centrifugation, oven dried and pulverized into a fine powder.

Preparation of alginate/hydroxyapatite composite beads

An aqueous solution of SA (2% w/v) was prepared in distilled water and mixed with 1% w/v of nHA powder. The composite mixture was homogenized by shaking at 500 rpm for 3 h. The zinc alginate/nanohydroxyapatite (ZA/nHA) beads were prepared by dropwise addition of the composite mixture into an aqueous solution of $ZnCl_2$ (0.1 M, 100 mL) and left to cross-link for 1 h at room temperature. The collected ZA/nHA beads were washed several times with distilled water and oven dried (60 °C).

Characterization of the developed nanocomposite

The morphology and particle size of nHA and the structure of the ZA/nHA were investigated using transmission electron microscope (JEOL JEM-100CX II) at the Electron Microscopy Unit, Assiut University. Fourier transform-infrared (FT-IR) spectra of the developed materials were obtained in the 4000–400 cm^{-1} region using a Nicolet IS 10 FT-IR spectrophotometer. The X-ray diffraction (XRD) analyses were performed using an X-ray diffractometer (Shimadzu XD-3A). The point of zero charge (pH_{pzc}) of the developed nanocomposite was determined as described in previous studies [20, 21].

Bacterial disinfection of synthetic-bacteria contaminated water

The antibacterial activity of the ZA/nHA composite for water disinfection was evaluated against *Escherichia coli* (OQ569760), as a common water and wastewater contaminant. The bacterial strain was inoculated into nutrient broth and incubated at 37 °C for 1–2 days. The cultivated cells were harvested by centrifugation (3800 g, 15 min) and resuspended in 0.9% (w/v) saline solution in sterile 100 mL Erlenmeyer flasks to give a final cell concentration of approximately 10^4, 10^5, and 10^6 CFU mL^{-1} (CFU: colony forming unit). Then, the ZA/nHA beads were added into the bacterial suspension at 0.2, 0.5, and 1% w/v, and the mixture was incubated at room temperature with shaking at 100 rpm using a reciprocal shaker. At predetermined time interval, aliquots of the treated bacterial samples were withdrawn and plated into nutrient agar after proper dilution. The plates were incubated at 37 °C in the dark for 24 h and the bacterial colonies were counted using a colony counter.

Repeated use of the ZA/nHA composite beads for bacterial disinfection

ZA/nHA composite beads was used to disinfect an *E. coli* suspension (10^4 CFU mL^{-1}) for 6 h at room temperature and 100 rpm. Afterwards, the ZA/nHA was collected by filtration, washed thrice with distilled water followed by 70% v/v ethanol for 5 s, and oven dried at 60 °C for 1 h. The collected ZA/nHA was used for the next cycle of the bacterial disinfection up to 7 cycles. After each cycle, aliquots of the bacterial suspension were diluted and plated on nutrient agar to check the viable residual cells.

Modelling of bacterial inactivation

The curves of *E. coli* disinfection (Log_{10} CFU mL^{-1} *vs.* time) were fitted to two kinetic equations: Log-linear [22] and Weibull model [23]. The equations of these models are as follows:

Log-linear: $Log_{10}(N_t) = Log_{10}(N_0) - K_{max}\frac{t}{Ln(10)}$
Weibull model: $Log_{10}(N_t) = Log_{10}(N_0) - \left(\frac{t}{\delta}\right)^P$

where K_{max} is disinfection rate constant. N_0 and N_t are the initial population of *E. coli* and the surviving population at time t. δ is a scale parameter reflecting the time required for 90% cell reduction (1 Log_{10}) of *E. coli* population. P is a shape parameter related to the curve shape as convex ($P > 1$), concave ($P < 1$) or linear ($P = 1$).

The two models were solved using Geeraerd Inactivation Model Fitting Tool (GInaFiT, v1.6) [24]. The comparison between the models was performed by comparing the coefficient of determination (R^2) and root mean sum of squared errors (RMSE).

Cyanobacterial and algal inactivation using ZA/nHA composite

The cyanobacterial cells of *Chroococcus* sp. and the green microalga *Chlorella* sp. were cultivated in Bold's Basal medium [25] under continuous illumination (48.4 µmol m^{-2}s^{-1}) at 25 °C with shaking (150 rpm). Algal cells were diluted using fresh medium to obtain an initial optical density at 750 nm of 0.2, then treated using 1% (w/v) of ZA/nHA beads in batch cultures. Control treatments without the composite beads were performed similarly. The algal growth inhibition was monitored daily by measuring

chlorophyll a (Chl. a) contents, which is a reliable indicator of cell viability during inactivation experiments [26]. A known aliquot of the microalgal suspension was withdrawn, and the cells were collected by centrifugation (3800 g, 15 min). The chlorophylls were extracted using 1 mL methanol at 60 °C, and the samples were recentrifuged. The absorbance of the supernatant was measured using a spectrophotometer at 653 and 666 nm and Chl. a contents were calculated using the following equation [27]:

$$Chl.a\left(\mu gmL^{-1}\right) = 15.65A_{666} - 7.34A_{653}$$

Adsorption of crystal violet using ZA/nHA composite

A known concentration of crystal violet (CV) was prepared in distilled water and mixed with a known amount of the ZA/nHA beads in 100 mL glass bottles. The initial pH of the CV solution was adjusted to 6.0 using diluted HCl or NaOH solutions. The adsorption experiment was maintained in the dark at 25 °C in a shaking incubator (150 rpm). An aliquot of the treated CV solution was withdrawn at predetermined time interval to determine the residual CV concentration. The concentration of the CV was determined by measuring the absorbance of the solution at its maximum wavelength (690 nm) using a spectrophotometer. The amount of CV adsorbed (q_t, mg g^{-1}) at time t (min) was estimated using the following equation:

$$q_t = \frac{(C_0 - C_t)V}{W}$$

where C_0 and C_t are the initial concentration of CV, and its residual concentration at time t, respectively. V represents the volume of the CV solution (L), and W is the weight of the adsorbent (g).

The adsorption of CV using the developed composite was investigated at different initial CV concentrations (2.5, 5, 10, and 20 mg L^{-1}), different temperatures (25, 35, and 45 °C), and different pH values (3, 4, 5, 6, 7, and 8).

Modeling of CV adsorption

The kinetics of the CV adsorption using ZA/nHA composite beads was simulated using the pseudo-first order (PFO), pseudo-second order (PSO), Elovich, and intra-particle diffusion (IPD) models using their non-linear equations.

PFO: $q_t = q_e\left(1 - e^{-k_1 t}\right)$
PSO: $q_t = \frac{k_2 q_e^2 t}{1 + k_2 q_e t}$
Elovich: $q_t = \frac{1}{\beta}\ln(1 + \alpha\beta t)$

IPD: $q_t = k_i t^{0.5} + C_i$ where q_t and q_e (mg g^{-1}) is the amount of CV adsorbed at time t and equilibrium,

respectively. k_1 (min^{-1}) and k_2 (g mg min^{-1}) are the rate constants for the PFO and PSO, respectively. α (mg g^{-1} min^{-1}) and β (g mg^{-1}) were related to the initial adsorption rate and the extent of surface coverage, respectively. K_i (mg g^{-1} min$^{-0.5}$) is the rate constant of the intra-particle diffusion and C_i (mg g^{-1}) is a constant reflecting the thickness of the boundary layer.

The adsorption process of CV was also investigated using different isotherm models viz. Langmuir, Freundlich, Sips, Dubinin-Radushkevich (D-R), and Temkin isotherms [28].

Langmuir: $q_e = \frac{q_m K_L C_e}{1 + K_L C_e}$
Freundlich: $q_e = K_F C_e^{1/n}$
Sips: $q_e = \frac{q_m K_S C_e^{1/n_S}}{1 + K_S C_e^{1/n_S}}$
D-R: $q_e = q_m e^{-\beta\varepsilon^2}$ and $\varepsilon = RT\ln\left(1 + \frac{1}{C_e}\right)$

Temkin: $q_e = \left(\frac{RT}{b_T}\right)\ln(A_T C_e)$ where q_m (mg g^{-1}) is the maximum amount of CV adsorbed by the ZA/nHA adsorbent. K_L (L mg^{-1}), K_F (mg g^{-1} (mg L^{-1})$^{-1/n}$), K_S (mg L^{-1})$^{-1/n}$, and A_T (L mg^{-1}) are the adsorption constants of the Langmuir, Freundlich, Sips, and Temkin isotherms, respectively. n and n_S are dimensionless exponents of the Freundlich and Sips isotherms, respectively. T (K) is the absolute temperature, and R (8.314 J mol^{-1} K^{-1}) is the universal gas constant. β (mol^2 J^{-2}) is a constant of adsorption energy, and ε (J mol^{-1}) is the Polanyi potential. b_T (J mol^{-1}) is a constant related to heat of adsorption.

Different kinetic and isotherm models were solved in Excel using Microsoft Solver function by minimizing the average relative error (%) (Eq. 1).

$$\%ARE = \frac{100}{N}\sum_{i=1}^{N}\left(\frac{|q_{pred} - q_{exp}|}{q_{pred}}\right) \tag{1}$$

where q_{pred} and q_{exp} refers to the predicted and the experimental amount of CV adsorbed, respectively. *N* represents the number of experimental points.

Additionally, temperature-dependent isotherms were used to investigate the thermodynamic process of CV adsorption based on the following equations [29]:

$$K_d = \frac{q_e}{C_e}$$

$$\Delta G° = -RT\ln K_d$$

$$\ln K_d = -\frac{\Delta H°}{RT} + \frac{\Delta S°}{R}$$

where K_d (L mg^{-1}) is the distribution coefficient. $\Delta G°$ (J mol^{-1}), $\Delta H°$ (J mol^{-1}), and $\Delta S°$ (J mol^{-1} K^{-1}) are the change of Gibbs free energy, enthalpy and entropy of the

adsorption process, respectively. R (8.314 J mol^{-1} K^{-1}) is the universal gas constant and T (K) is the absolute temperature. The plot (ln K$_d$ *vs.* 1/T) was used to calculate the ΔH° and ΔS° by linear regression.

Results and discussion

A novel cost-effective and sustainable Zn^{2+}-crosslinked alginate/nanohydroxyapatite (ZA/nHA) composite was developed based on the brown macroalga *S. latifolium* as a source of alginate and the calcified red macroalga *T. fragilis* as a material for hydroxyapatite synthesis (Fig. S1). The extracted alginate had a viscosity average molecular weight of 1.76×10^5 Da and mannuronic/guluronic acid ratio of 1.79. The pH$_{pzc}$ of the developed ZA/nHA beads was 6.55.

FT-IR analysis

The hydrogen bonded O−H and C-H stretching vibrations in the macroalgal-derived alginate were observed at 3427.52 and 2929.69 cm^{-1}, respectively (Fig. 1a). The sharp bands centered at 1621.46 and 1411.24 cm^{-1} were attributed to the asymmetric and symmetric −COO$^-$ vibrations, respectively [30, 31]. While the C−C stretching vibration was located at 1452.25 cm^{-1}. Furthermore, the stretching vibrations of C−O bonds were located at 1126.10 cm^{-1} and 1028.75 cm^{-1}, while that at 1095.11 cm^{-1} indicated both C−O and C−C stretching vibrations [31]. The alginate spectrum exhibited a specific band of uronic acid at 947.44 cm^{-1} which was attributed to the C−O stretching vibrations (Fig. S1 b). Similarly, the bands at 904.65 and 839.97 cm^{-1} were assigned to the α-guluronic and β-mannuronic acid, respectively [31]. The band at 868.32 cm^{-1} was related to the C1-H deformation vibration of β-mannuronic acid [30].

On the other hand, the FT-IR spectrum of the phycogenic nHA (Fig. 1b) indicated the existence of strong and sharp peak centered at 1035.09 cm^{-1} (ν$_3$), and two weak peaks at 1099.27 cm^{-1} (ν$_3$) and 961.38 cm^{-1} (ν$_1$) were attributed to PO$_4^{3-}$ ions (stretching vibration of the P−O−P bond). The splitting sharp peaks at 602.94 and 564.02 cm^{-1} (ν$_4$) reflected bending vibration of the PO$_4^{3-}$ ions, which occupied two sites in the crystal lattice [32]. Furthermore, the asymmetric stretching vibration of PO$_4^{3-}$ was indicated by a weak peak at 472.01 cm^{-1} (ν$_2$) [33]. The stretching vibrations of the OH$^-$ groups were assigned to the broad band at 3424.04 cm^{-1}, with the band at 1640.71 cm^{-1} indicating the adsorbed or bounded H$_2$O. Additionally, the presence of weak band at 873.79, 1413.89, and 1458.76 cm^{-1} may be assigned to CO$_3^{2-}$ anions substituting for the PO$_4^{3-}$ in the hydroxyapatite lattice (B-type hydroxyapatite) [34]. The carbonate that existed in the nHA was attributed to the adsorbed CO$_2$

from the air, since the CaCO$_3$ present in the seaweed biomass was solubilized using HCl during the first steps of nHA synthesis. Moreover, the existence of double sharp bands 564.02/602.94 and 1035.09/1099.27 cm^{-1} in the algal-derived n-HA reflected a high degree of crystallinity [33, 34].

The FT-IR spectrum of the ZA/nHA composite was depicted in Fig. 1c. New peaks located at 1624.48, 1423.72 and 1321.54 cm^{-1} were assigned to the COO$^-$ groups of alginate and the one at 817.11 cm^{-1} may be identified as the combination of three possible vibrational modes (τ(CO)+δ(CCO)+δ(CCH)) of Zn-alginate [16]. Moreover, the shift in the COO$^-$ groups in the composite compared to sodium alginate reflected the presence of electrostatic interactions and bond formation between the positively charged Ca^{2+} in the hydroxyapatite and COO$^-$ groups of alginate [35]. In general, the FT-IR analysis confirmed a successful utilization of macroalgae wastes as cost-effective and sustainable approach for the fabrication of nanocomposite based on alginate and hydroxyapatite.

XRD analysis

The XRD spectrum (Fig. 2a) of Na-alginate exhibited a distinctive peak between (2θ) 20° to 30°, which could be related to the amorphous nature of the polymer network [19, 36, 37]. The algal-derived nHA exhibited numerous peaks in the XRD spectrum (Fig. 2b), which were perfectly matched with standard card JCPDS: 01–074-0565 and indicates the formation of single phase of hydroxyapatite with the chemical formula Ca$_{10}$(PO$_4$)$_6$(OH)$_2$. Furthermore, the developed nHA showed hexagonal structure with a space group number 176 and a space group category P6$_3$/m. The average crystallite size of nHA was 41.88 nm based on the Debye–Scherrer equation [16]. This size is quite similar to the nHA prepared from other natural sources such as bone [17], and egg shell [38].

On the other side, the spectrum of ZA/nHA beads exhibited characteristic peaks for both alginate and nHA (Fig. 2c). However, the spectrum of ZA/nHA indicated a shift and decrease in intensity of the major peaks for pure nHA and alginate, which implied the successful interaction between the nHA particles and alginate network.

TEM analysis

Figure 3a depicts the TEM of the algal-derived hydroxyapatite. It was observed that the nHA particles had elongated ellipsoid-like shape. The crystallite size from TEM images using ImageJ software was 42.46±17.92 nm. The TEM image of ZA/nHA beads showed the presence of agglomeration of nHA crystallites within the alginate matrix (Fig. 3b).
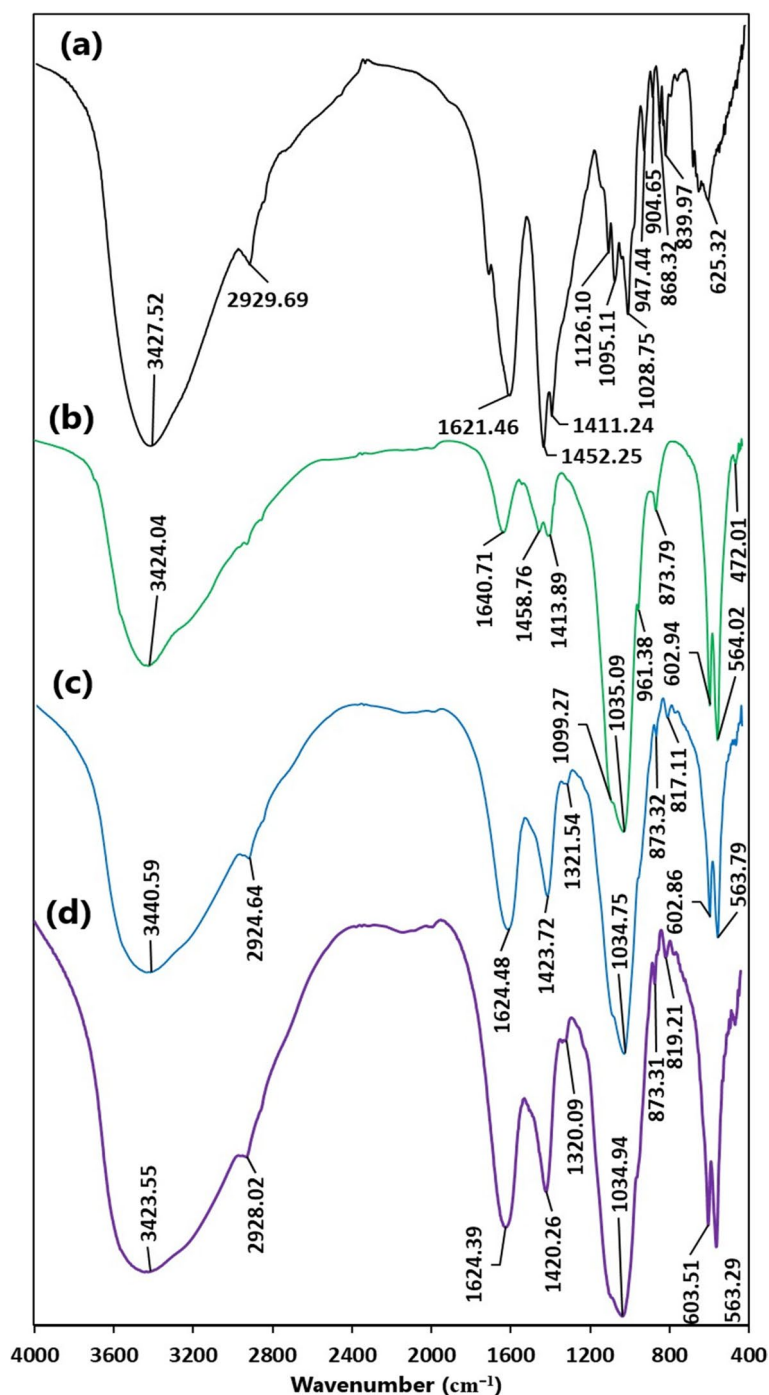
Fig. 1 FT-IR spectra of (**a**) alginate from *S. latifolium*, (**b**) nanohydroxyapatite synthesized using *T. fragilis* biomass, (**c**) zinc alginate / nanohydroxyapatite composite, and (**d**) zinc alginate / nanohydroxyapatite composite after the adsorption of crystal violet

Leaching of Zn^{2+} from the nanocomposite

The leaching of Zn^{2+} from the developed nanocomposite is of great importance, since it could influence its stability and application in water treatment as well as its environmental and health effects. As depicted in Fig. S2, the

amount of Zn^{2+} released from the ZA/nHA composite was 1.50 and 2.16 mg L^{-1} after 6 and 24 h, respectively. The content of Zn^{2+} released remained relatively constant after 24 h. These values were generally lower than the maximum allowable concentration of $3 - 5$ Zn^{2+} mg
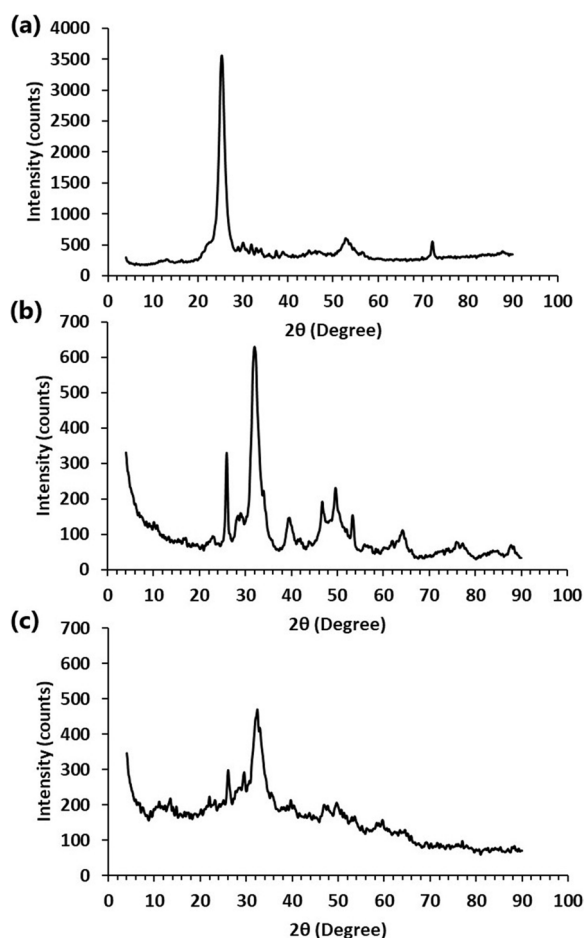
Fig. 2 XRD spectra of (**a**) alginate, (**b**) nanohydroxyapatite, and (**c**) zinc alginate/nanohydroxyapatite composite

L^{-1} in drinking water suggested by WHO [1]. This result implied the safe use of the developed ZA/nHA composite for the treatment of water.

Bacterial removal from contaminated water

The antibacterial activity of the developed ZA/nHA nanocomposite was tested against *E. coli*, a common pathogen in contaminated water (Fig. S3). The results depicted in Fig. 4 indicated that ZA/nHA exhibited concentration-dependent antibacterial activity. The effective disinfection of *E. coli* was related to the initial concentration of bacterial cells as well as the nanocomposite dosage.

The survival curves of *E. coli* in the presence of ZA/nHA nanocomposite were fitted to the Log-linear and the Weibull models (Table 1). Based on the R^2 and RMSE values, the Weibull equation exhibited better fitting to the experimental results than the Log-linear equation. The inactivation kinetics of *E. coli* by the ZA/nHA are in good consistent with those of thermally-inactivated bacteria, which can also best described by the Weibull equation [39, 40]. The shape parameter (P) of the Weibull equation reflected downward concavity (*P* > 1), when the initial population of *E. coli* was ~10^4 and 10^5 CFU mL^{-1} (Table 1). Conversely, when the bacterial concentration was increased to ~10^6 CFU mL^{-1}, an upward concavity (*P* < 1) of the survival curve was evident except at 1% w/v of Zn/nHA, the curve was linear (*P* = 1) (Table 1). These empirical values could also reflect physiological effects of the nanocomposite on bacterial cells. At *P* > 1, the remaining cells of *E. coli* were increasingly damaged, while at *P* < 1, the cells may adapt to the applied stress [39]. These observations implied the effectiveness of the developed ZA/nHA composite in the disinfection of *E.*
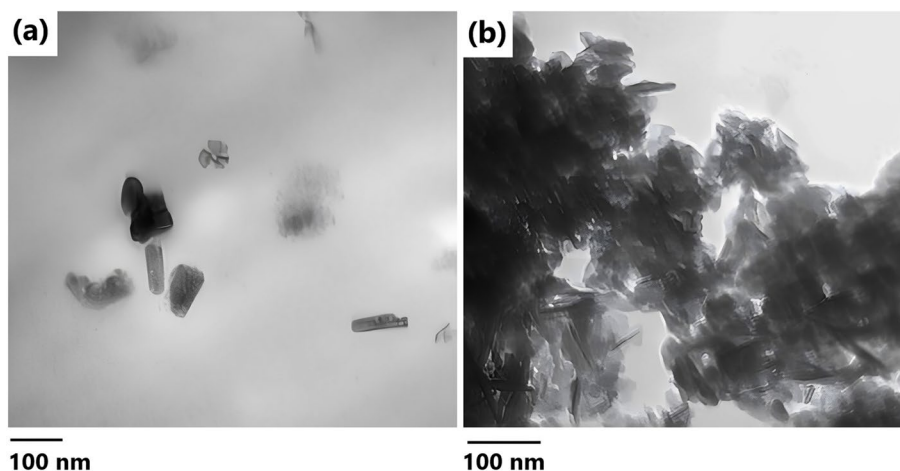

Fig. 3 TEM images of (**a**) nanohydroxyapatite and (**b**) zinc alginate/ nanohydroxyapatite composite
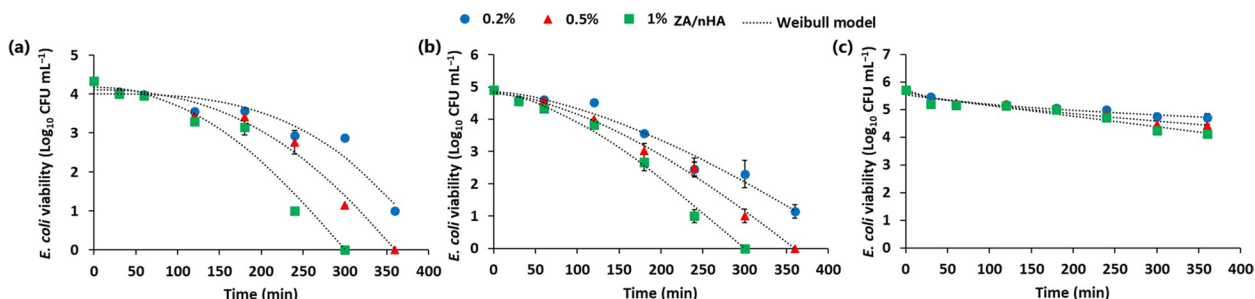
Fig. 4 Kinetics of *E. coli* disinfection using different concentrations of zinc alginate/ nanohydroxyapatite beads at different initial bacterial concentrations of (**a**) 10^4, (**b**) 10^5, and (**c**) 10^6 CFU mL.$^{-1}$

Table 1 Kinetic modelling of bacterial disinfection under different treatments using Log-linear and Weibull models

ZA/nHA (% w/v)	CFU mL^{-1}	Log-linear model			Weibull modell			
		K_{max}	R^2	RMSE	δ	β	R^2	RMSE
0.2	10^4	0.02	0.831	0.47	254.95	3.02	0.926	0.34
	10^5	0.02	0.945	0.35	152.05	1.52	0.972	0.28
	10^6	0.01	0.903	0.11	370.62	0.50	0.969	0.07
0.5	10^4	0.03	0.892	0.55	195.13	2.33	0.981	0.25
	10^5	0.03	0.964	0.37	131.86	1.57	0.993	0.18
	10^6	0.01	0.929	0.13	282.03	0.73	0.937	0.13
1.0	10^4	0.03	0.905	0.56	144.33	1.99	0.967	0.37
	10^5	0.04	0.964	0.39	105.99	1.54	0.991	0.22
	10^6	0.01	0.919	0.16	257.36	1.00	0.919	0.18

K_{max}: disinfection rate constant. δ: scale parameter reflecting the time required for 90% cell reduction (1 Log$_{10}$) of *E. coli* population. P is a shape parameter. R2: coefficient of determination. RMSE: root mean square error

coli-contaminated water at populations $\leq 10^5$ CFU mL^{-1}. Higher bacterial populations require prolonged treatment and/or higher composite dosage for effective disinfection.

Cyanobacterial and algal removal from water

The effective removal of *Chroococcus* sp. and *Chlorella* sp. from water by ZA/nHA beads was monitored daily by measuring the concentration of Chl. a. The results depicted in Fig. 5 clearly demonstrated that ZA/nHA eliminated nearly 100% of *Chroococcus* sp. cells after 2 days of treatment. Conversely, the removal of *Chlorella* sp. reached ~90% after 4 days of treatment. More importantly, neither *Chroococcus* sp. nor *Chlorella* sp. was able to regrow after removing the beads and cultivation in a new medium.

Adsorption of CV using ZA/nHA nanocomposite

The developed ZA/nHA nanocomposite exhibited fast adsorption properties towards CV (Fig. 6a). Accordingly, the nanocomposite adsorbed 0.11 mg g^{-1} of CV after 0.5 min and the maximum adsorbed amount was 0.17 mg g^{-1} at 7 min. However, a small degree of desorption was observed at prolonged contact time (Fig. 6a). Similarly,

the adsorption of methylene blue using sodium alginate/ hydroxyapatite composite was fast and the equilibrium was attained within short period (30 min) [16].

The kinetic mechanism of CV adsorption was evaluated using different kinetic equations and the results are listed in Table 2. The best fitting of the models was arbitrated based on high coefficient of determination (R^2), and low error (%ARE). The results indicated that the PSO and Elovich equations better described the kinetics of CV adsorption on the surface of ZA/nHA than the PFO model (Fig. 6a, Table 2). The calculated equilibrium adsorption capacity ($q_e = 0.178$ mg g^{-1}) by the PSO exhibited satisfactory fitting the experimental value ($q_e = 0.171$ mg g^{-1}). The PSO model assumes that chemical adsorption is a rate-controlling mechanism for the removal of CV by ZA/nHA from aqueous solution. Similarly, Elovich model describes chemisorption and assumes that the adsorbent have heterogenous binding sites with various binding energies [41].

The kinetics of CV removal were also fitted to the intra-particle diffusion model to determine the rate limiting step, and the results were depicted in Fig. 6b. The high R^2 of the first linear region in the plot (q_t *vs* $t^{0.5}$) deviated from
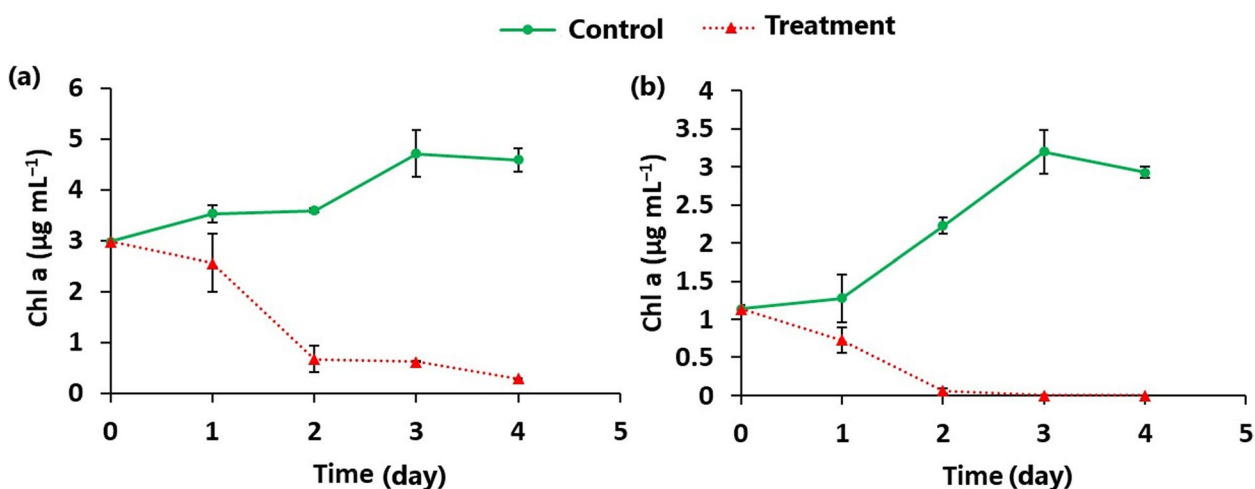
Fig. 5 Time-dependent variations in Chl. a concentration of (**a**) *Chlorella* sp. and (**b**) *Chroococcus* sp. after treatment with 1% w/v of zinc alginate/nanohydroxyapatite beads in relation to the untreated control
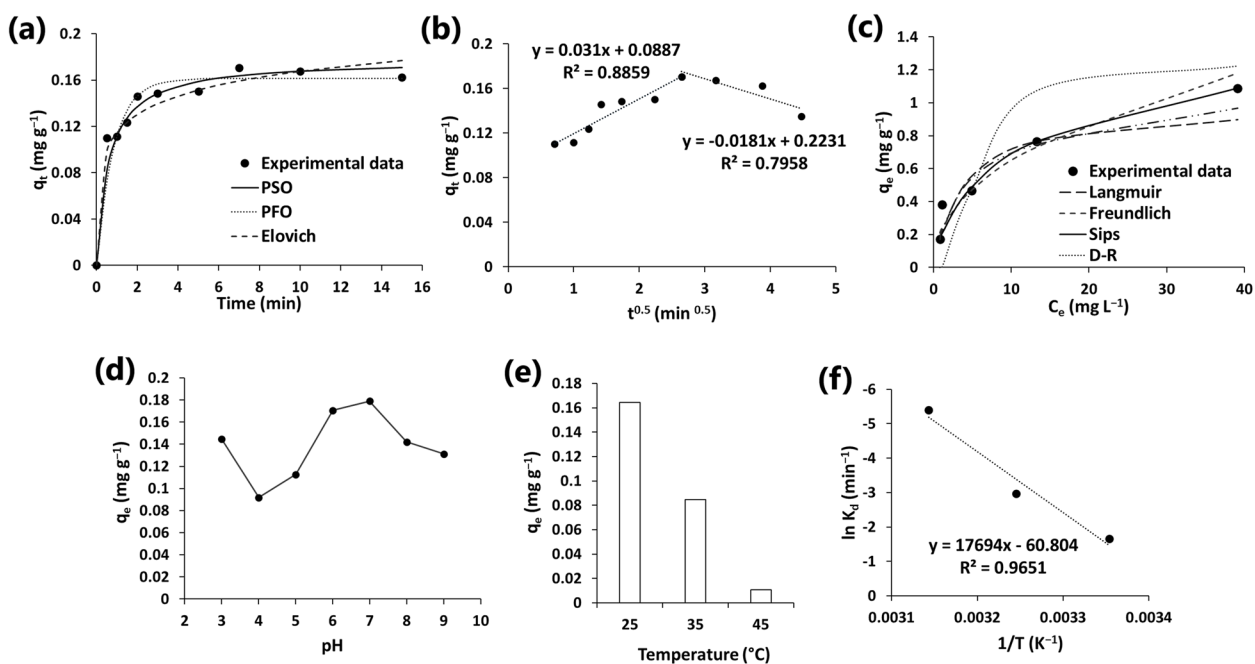

Fig. 6 **a** Kinetics of crystal violet (CV) removal and fitting to pseudo-first order (PFO), pseudo-second order (PSO) and Elovich equations. **b** Kinetics modelling of CV adsorption using intra-particle diffusion model. **c** Effect of different initial CV concentrations on the adsorption process and fitting to different isotherm models. **d** Effect of pH on CV adsorption. **e** Effect of temperature on CV adsorption. **f** Thermodynamic plot for CV adsorption

the origin (Table 2). This implied that the intra-particle diffusion was prominent, but the deviation of the plot from the origin indicated a significant effect of the external mass transfer. The second linear region was related to the desorption of CV. The intra-particle rate constant (K_i) was low in the second linear region, which reflected a slow desorption process in relation to the fast adsorption process.

The adsorption process of CV was also evaluated using different isotherms (Table 2, Fig. 6c). The investigated models exhibited satisfactory fitting to the experimental data, but the best fit was related to the Sips model, owing to relatively low %ARE values (Table 3). In general, the Sips model combines the assumptions of both Langmuir and Freundlich models [28]. The Langmuir model

Table 2 Different parameters for the pseudo-first order (PFO), pseudo-second order (PSO), and Elovich models for the biosorption of crystal violet using zinc alginate/ nanohydroxyapatite beads

Models	Parameters	
Experimental	q_e (mg g^{-1})	0.171
PFO	K_1 (min^{-1})	1.18
	q_e (mg g^{-1})	0.161
	R^2	0.780
	%ARE	9.36
PSO	q_e (mg g^{-1})	0.178
	K_2(g mg^{-1} min^{-1})	9.50
	R^2	0.878
	%ARE	5.60
Elovich	β (g mg^{-1})	43.08
	α (mgg^{-1} min^{-1})	3.16
	R^2	0.868
	%ARE	5.15

Table 3 Calculated parameter for different isotherm models for the adsorption of crystal violet using zinc alginate/ nanohydroxyapatite beads

Models	Parameters	
Langmuir	q_m (mg g^{-1})	0.982
	K_L (L mg^{-1})	0.26
	R_L	0.07 – 0.60
	R^2	0.891
	%ARE	15.80
Freundlich	N (mg g^{-1}) (L mg^{-1})$^{1/n}$	2.25
	K_F (mg g^{-1})	0.23
	R^2	0.960
	%ARE	14.62
Sips	q_m (mg g^{-1})	1.74
	n_s	1.42
	K_s (mg L^{-1}) $^{-1/n}$	0.13
	R^2	0.959
	%ARE	10.02
D-R	q_m (mg g^{-1})	1.25
	β (mol^2 J^{-2})	4.57×10^{-6}
	E (kJ mol^{-1})	0.33
	R^2	0.892
	%ARE	50.58
Temkin	A_T (L mg^{-1})	2.89
	b_T (kJ mol^{-1})	12.11
	R^2	0.935
	%ARE	13.69

assumes the formation of a monolayer of the adsorbate molecules, which is chemically adsorbed at energetically homogenous sites [42]. However, the presence of different functional groups on the surface of ZA/nHA indicated their heterogenous behavior towards CV, which violates the basic principle of Langmuir model. Conversely, the assumption of the Freundlich model is related to the formation of multilayer of the adsorbate molecules at energetically different binding sites. At low pollutant concentrations, the Sips equation relatively reduces to the Freundlich model, but it can describe the monolayer coverage of the Langmuir model at high pollutant concentrations [28].

An important parameter of the Langmuir isotherm is a dimensionless separation factor (R_L), which is obtained as follows:

$$R_L = \frac{1}{1 + K_L C_0}$$

where K_L is the Langmuir constant and C_0 is the initial CV concentration. This parameter signifies adsorption as unfavorable ($R_L > 1$), linear ($R_L = 1$), favorable ($0 < R_L < 1$), or irreversible ($R_L = 0$) [10]. The calculated R_L values in the present study fluctuated between 0.07 and 0.6 (Table 3), which implied favorable CV adsorption. In addition, the lower R_L values were observed at high CV concentration, which reflected that the adsorption process became more favorable at high CV concentrations. The dimensionless exponent of Freundlich model (n) can also be used to describe the nature of the adsorption as ($n = 1$), physical ($n > 1$), or chemical ($n < 1$) [41]. The n value for CV adsorption was 2.25 (Table 3), which demonstrated the heterogenous nature of the developed adsorbent and signified the adsorption of CV as favorable physical process. The existence of various binding sites with different binding energies was also supported by the satisfactory fitting of the Temkin isotherm. The b_T values of the Temkin model was 12.11 kJ mol^{-1}, which is lower than 20 kJ mol^{-1}, which is a characteristic feature of exothermic physical adsorption [43].

On the other side, the D-R isotherm showed the highest %ARE among the tested isotherms, suggesting a poor fitting to the experimental data. An essential property of the D-R isotherm is the calculation of mean free energy (E, kJ mol^{-1}) of the adsorption using the following expression:

$$E = \frac{1}{\sqrt{2\beta}}$$

The E values signifies the adsorption process as chemical (E > 16 kJ mol^{-1}), or physical (E < 8 kJ mol^{-1}). The estimated E value for CV adsorption in the present study is 0.33 kJ mol^{-1} (Table 3), which indicated that the process is more inclined into physisorption.

On the other hand, pH of the solution during the adsorption process is a crucial parameter since it directly

influences the surface charges of both adsorbent and adsorbate molecules. The effects of pH on the adsorption process of CV were depicted in Fig. 6d. The results indicated a maximum adsorption of CV at pH 6–7. The pH_{pzc} of the developed ZA/nHA beads was 6.55, which indicated its existence as a positively charged adsorbent at $pH < pH_{pzc}$. Accordingly, increasing the pH enables the adsorption of ^-OH ions on the surface of ZA/nHA beads, making it negatively charged and thus the removal of CV increased as a result of electrostatic interactions. However, the slight increase of CV adsorption at pH 3 may indicate that the adsorption is hydrogen-bonded controlled. The enhancement in the adsorption capacity of cationic dyes with the increasing pH agreed with previous studies [44].

Increasing temperature during adsorption markedly decreases the ability of the ZA/nHA to remove CV (Fig. 6e, f). The orientation and mechanism of CV adsorption was further investigated using thermodynamic parameters. The ΔH^o value obtained in the current study for CV adsorption was negative, which is related to exothermic adsorption. The decrease of randomness at the adsorbent/adsorbate interface was indicated by the negative ΔS^o value. Besides, the negative ΔS^o suggested an associative adsorption mechanism without changes in the internal structure of the nanocomposite [29]. While the negative values of ΔG^o signified the spontaneity of the thermodynamically favorable adsorption. The magnitude of ΔG^o can also be used to identify adsorption mechanism as physisorption (ΔG^o: -20 to 0 kJ mol^{-1}) or chemisorption (ΔG^o: -80 to -400 kJ mol^{-1}). Accordingly, the listed ΔG^o values in Table S1 indicated that the adsorption of CV on the surface of ZA/nHA is physical, which agreed with the results of the D-R model. In a similar study, the adsorption of methylene blue was predominately physical on the surface of sodium alginate/hydroxyapatite material [16].

The FT-IR analysis of the nanocomposite beads after the adsorption of CV indicated a marked shift in the O–H stretching vibrations into lower wavenumber (3423.55 cm^{-1}). Similarly, the peak of symmetric $-COO^-$ vibrations was slightly shifted into lower wavenumber (1420.26 cm^{-1}). Furthermore, A slight shift to the higher wavenumber was observed in the peaks of C-H (2928.09 cm^{-1}), PO_4^{3-} (603.51 cm^{-1}), and the three vibrational modes of $\tau(CO) + \delta(CCO) + \delta(CCH)$ (819.21 cm^{-1}). The shift in these functional groups in the nanocomposite implied their potential role in the removal of CV. The hydrogen-donating groups such as OH and COOH in the ZA/nHA adsorbent may form H-bonding interactions with the hydrogen accepting group (nitrogen) of CV. Furthermore, another type of H-bonding may occur between the H-donating groups of the adsorbent and the aromatic rings of CV, which is known as Yoshida bonding [10, 11]. Similarly, the presence of electron- donating oxygen groups in the ZA/nHA may induce the formation of n-π interaction with aromatic rings of CV as electron-acceptor. Furthermore, the electrostatic interactions were also evident as indicated by the effects of pH on the removal process.

Conclusion

A novel cost-effective multi-functional composite was developed using alginate from the brown seaweed *S. latifolium* and hydroxyapatite synthesized by chemical precipitation using the red seaweed *T. fragilis* as $CaCO_3$ source. The developed ZA/nHA was effectively applied to disinfect *E. coli* in water and the efficiency was increased by increasing the composite concentration and decreasing bacterial load. The kinetics of bacterial disinfection exhibited good fitting to the Weibull equation. Furthermore, the ZA/nHA showed potential application in the removal of cyanobacterial cells and microalgae after 2–3 days of treatment. On the other side, the developed composite showed fast adsorption removal of CV from the solution with q_e value equal to 0.171 mg g^{-1} within 7 min. The adsorption process was maximized at pH 6–7 which is suitable for the treatment of dye-polluted water without pH adjustment. The PSO and Elovich equations exhibited better fitting to the kinetics of CV adsorption than the PFO model. While the isotherm analysis indicated better fitting of the Sips model than Langmuir and Freundlich equations. The adsorption process was more inclined into physiosorption through H-bonding, Yoshida-boding, and n-π interactions and became more favorable at high concentration of CV. The results of the present study highlighted the promising application of sustainable macroalgae biomass for the development of cost-effective nanocomposite for the treatment of both drinking water and wastewater.

Supplementary Information

Additional file 1.

Authors' contributions
M. Gomaa: Conceptualization, Validation, Investigation, Methodology, Formal analysis, Writing—original draft, Writing—review & editing. A. W. Danial: Validation, Investigation, Methodology, Writing - review & editing.

Declarations

Ethics approval and consent to participate

Not applicable.

Consent for publication

Not applicable.

Conflict of interest

The authors declare no conflict of interest.

Competing interests

The authors declare no competing interests.

Author details

[1]Botany & Microbiology Department, Faculty of Science, Assiut University, Assiut 71516, Egypt.

References

1. WHO. World Health Organization: Guidelines for Drinking-water Quality. Vol. 1: Fourth edi. Geneva: World Health Organization; 2011.
2. Epa. National Primary Drinking Water Regulations. New York, NY, USA: Environmental Protection Agency (May 2009 816-F-09–004); 2009.
3. Gobler CJ. Climate Change and Harmful Algal Blooms: Insights and perspective. Harmful Algae. 2020;91: 101731. https://doi.org/10.1016/j.hal.2019.101731.
4. Solanki S, Sinha S, Bisaria K, Singh R, Saxena R. Accurate data prediction by fuzzy inference model for adsorption of hazardous azo dyes by novel algal doped magnetic chitosan bionanocomposite. Environ Res. 2022;214: 113844. https://doi.org/10.1016/j.envres.2022.113844.
5. Isik B, Avci S, Cakar F, Cankurtaran O. Adsorptive removal of hazardous dye (crystal violet) using bay leaves (Laurus nobilis L.): surface characterization, batch adsorption studies, and statistical analysis. Environ Sci Pollut Res. 2023;30:1333–56. https://doi.org/10.1007/s11356-022-22278-4
6. Chakraborty S, Chowdhury S, Das SP. Adsorption of Crystal Violet from aqueous solution onto NaOH-modified rice husk. Carbohydr Polym. 2011;86:1533–41. https://doi.org/10.1016/j.carbpol.2011.06.058.
7. Richardson SD, Postigo C. Drinking Water Disinfection By-products. 2011. p. 93–137. https://doi.org/10.1007/698_2011_125.
8. Boorman GA. Drinking water disinfection byproducts: review and approach to toxicity evaluation. Environ Health Perspect. 1999;107:207–17. https://doi.org/10.1289/ehp.99107s1207.
9. Shabir M, Yasin M, Hussain M, Shafiq I, Akhter P, Nizami A-S, et al. A review on recent advances in the treatment of dye-polluted wastewater. J Ind Eng Chem. 2022;112:1–19. https://doi.org/10.1016/j.jiec.2022.05.013.
10. Fawzy MA, Gomaa M. Low-cost biosorption of Methylene Blue and Congo Red from single and binary systems using Sargassum latifolium biorefinery waste/wastepaper xerogel: an optimization and modeling study. J Appl Phycol. 2021;33:675–91. https://doi.org/10.1007/s10811-020-02290-2.
11. Fawzy MA, Gomaa M. Use of algal biorefinery waste and waste office paper in the development of xerogels: A low cost and eco-friendly biosorbent for the effective removal of congo red and Fe (II) from aqueous solutions. J Environ Manage. 2020;262:110380.
12. Gomaa M. Biodegradable Plastics Based on Algal Polymers: Recent Advances and Applications. Handb Biodegrad Mater. Cham: Springer International Publishing; 2022. p. 1–31. https://doi.org/10.1007/978-3-030-83783-9_20-1
13. Fawzy MA, Gomaa M. Optimization of citric acid treatment for the sequential extraction of fucoidan and alginate from Sargassum latifolium and their potential antioxidant and Fe(III) chelation properties. J Appl Phycol 2021 334. 2021;33:2523–35. https://doi.org/10.1007/S10811-021-02453-9
14. Oliveira JM, Grech JMR, Leonor IB, Mano JF, Reis RL. Calcium-phosphate derived from mineralized algae for bone tissue engineering applications. Mater Lett. 2007;61:3495–9. https://doi.org/10.1016/j.matlet.2006.11.099.
15. Saxena V, Shukla I, Pandey LM. Hydroxyapatite: an inorganic ceramic for biomedical applications. Mater Biomed Eng. Elsevier; 2019. p. 205–49. https://doi.org/10.1016/B978-0-12-816909-4.00008-7
16. Guesmi Y, Agougui H, Lafi R, Jabli M, Hafiane A. Synthesis of hydroxyapatite-sodium alginate via a co-precipitation technique for efficient adsorption of Methylene Blue dye. J Mol Liq. 2018;249:912–20. https://doi.org/10.1016/j.molliq.2017.11.113.
17. Googerdchian F, Moheb A, Emadi R. Lead sorption properties of nano-hydroxyapatite–alginate composite adsorbents. Chem Eng J. 2012;200–202:471–9. https://doi.org/10.1016/j.cej.2012.06.084.
18. Sekar S, Panchu SE, Kolanthai E, Rajaram V, Subbaraya NK. Enhanced stability of hydroxyapatite/sodium alginate nanocomposite for effective fluoride adsorption. Mater Today Proc. 2022;58:909–17. https://doi.org/10.1016/j.matpr.2021.12.064.
19. Gholizadeh BS, Buazar F, Hosseini SM, Mousavi SM. Enhanced antibacterial activity, mechanical and physical properties of alginate/hydroxyapatite bionanocomposite film. Int J Biol Macromol. 2018;116:786–92. https://doi.org/10.1016/j.ijbiomac.2018.05.104.
20. Khan TA, Nazir M, Khan EA. Adsorptive removal of rhodamine B from textile wastewater using water chestnut (Trapa natans L.) peel: adsorption dynamics and kinetic studies. Toxicol Environ Chem. 2013;95:919–31.
21. Bisaria K, Singh R, Gupta M, Mathur A, Dixit A. Novel acoustic-activated alkali-functionalized Trapa bispinosa peel biochar for green immobilization of chlorpyrifos from wastewater: artificial intelligence modelling and experimental validation. Biomass Convers Biorefinery. 2022. https://doi.org/10.1007/s13399-022-02898-z.
22. Bigelow WD, Esty JR. The thermal death point in relation to time of typical thermophilic organisms. J Infect Dis. 1920;27:602–17.
23. Mafart P, Couvert O, Gaillard S, Leguerinel I. On calculating sterility in thermal preservation methods: application of the Weibull frequency distribution model. Int J Food Microbiol. 2002;72:107–13. https://doi.org/10.1016/S0168-1605(01)00624-9.
24. Geeraerd AH, Valdramidis VP, Van Impe JF. GInaFiT, a freeware tool to assess non-log-linear microbial survivor curves. Int J Food Microbiol. 2005;102:95–105. https://doi.org/10.1016/j.ijfoodmicro.2004.11.038.
25. Bischoff HW, Bold HC. Some soil algae from enchanted rock and related algae species. Phycol. Stud. IV. Univ. Texas Publ. No. 6318. Austin, Texas: University of Texas Publ; 1963.
26. Baniamerian H, Tsapekos P, Alvarado-Morales M, Shokrollahzadeh S, Safavi M, Angelidaki I. Anti-algal activity of Fe2O3–TiO2 photocatalyst on Chlorella vulgaris species under visible light irradiation. Chemosphere. 2020;242:125119. https://doi.org/10.1016/j.chemosphere.2019.125119.
27. Lichtenthaler HK, Wellburn AR. Determinations of total carotenoids and chlorophylls a and b of leaf extracts in different solvents. Biochem Soc Trans. 1983;11:591–2. https://doi.org/10.1042/bst0110591.
28. Lima ÉC, Adebayo MA, Machado FM. Kinetic and Equilibrium Models of Adsorption. 2015. p. 33–69. https://doi.org/10.1007/978-3-319-18875-1_3
29. Saha P, Chowdhury S. Insight Into Adsorption Thermodynamics. Thermodynamics. InTech; 2011. https://doi.org/10.5772/13474
30. Leal D, Matsuhiro B, Rossi M, Caruso F. FT-IR spectra of alginic acid block fractions in three species of brown seaweeds. Carbohydr Res. 2008;343:308–16. https://doi.org/10.1016/j.carres.2007.10.016.
31. Fawzy MA, Gomaa M, Hifney AF, Abdel-Gawad KM. Optimization of alginate alkaline extraction technology from Sargassum latifolium and its potential antioxidant and emulsifying properties. Carbohydr Polym. 2017;157:1903–12.
32. Ślósarczyk A, Paszkiewicz Z, Paluszkiewicz C. FTIR and XRD evaluation of carbonated hydroxyapatite powders synthesized by wet methods. J Mol Struct. 2005;744–747:657–61. https://doi.org/10.1016/j.molstruc.2004.11.078.
33. Youness RA, Taha MA, Elhaes H, Ibrahim M. Molecular modeling, FTIR spectral characterization and mechanical properties of carbonated-hydroxyapatite prepared by mechanochemical synthesis. Mater Chem Phys. 2017;190:209–18. https://doi.org/10.1016/j.matchemphys.2017.01.004.
34. Prekajski M, Mirković M, Todorović B, Matković A, Marinović-Cincović M, Luković J, et al. Ouzo effect—New simple nanoemulsion method for

synthesis of strontium hydroxyapatite nanospheres. J Eur Ceram Soc. 2016;36:1293–8. https://doi.org/10.1016/j.jeurceramsoc.2015.11.045.

35. Parhi P, Ramanan A, Ray AR. Preparation and characterization of alginate and hydroxyapatite-based biocomposite. J Appl Polym Sci. 2006;102:5162–5. https://doi.org/10.1002/app.24706.

36. Maity S, Mukhopadhyay P, Kundu PP, Chakraborti AS. Alginate coated chitosan core-shell nanoparticles for efficient oral delivery of naringenin in diabetic animals—An in vitro and in vivo approach. Carbohydr Polym. 2017;170:124–32. https://doi.org/10.1016/j.carbpol.2017.04.066.

37. Tohamy KM, Mabrouk M, Soliman IE, Beherei HH, Aboelnasr MA. Novel alginate/hydroxyethyl cellulose/hydroxyapatite composite scaffold for bone regeneration: In vitro cell viability and proliferation of human mesenchymal stem cells. Int J Biol Macromol. 2018;112:448–60. https://doi.org/10.1016/j.ijbiomac.2018.01.181.

38. Wu S-C, Hsu H-C, Wang H-F, Liou S-P, Ho W-F. Synthesis and Characterization of Nano-Hydroxyapatite Obtained from Eggshell via the Hydrothermal Process and the Precipitation Method. Molecules. 2023;28:4926. https://doi.org/10.3390/molecules28134926.

39. van Boekel M. On the use of the Weibull model to describe thermal inactivation of microbial vegetative cells. Int J Food Microbiol. 2002;74:139–59. https://doi.org/10.1016/S0168-1605(01)00742-5.

40. Zhang D, Yan S, Song W. Photochemically Induced Formation of Reactive Oxygen Species (ROS) from Effluent Organic Matter. Environ Sci Technol. 2014;48:12645–53. https://doi.org/10.1021/es5028663.

41. Hifney AF, Zien-Elabdeen A, Adam MS, Gomaa M. Biosorption of ketoprofen and diclofenac by living cells of the green microalgae Chlorella sp. Environ Sci Pollut Res. 2021;28:69242–52.

42. Danial AW, Dardir FM. Copper biosorption by Bacillus pumilus OQ931870 and Bacillus subtilis OQ931871 isolated from Wadi Nakheil, Red Sea. Egypt Microb Cell Fact. 2023;22:152. https://doi.org/10.1186/s12934-023-02166-3.

43. Soltani R, Marjani A, Shirazian S. Facile one-pot synthesis of thiol-functionalized mesoporous silica submicrospheres for Tl(I) adsorption: Isotherm, kinetic and thermodynamic studies. J Hazard Mater. 2019;371:146–55. https://doi.org/10.1016/j.jhazmat.2019.02.076.

44. Parisi F. Adsorption and Separation of Crystal Violet, Cerium(III) and Lead(II) by Means of a Multi-Step Strategy Based on K10-Montmorillonite. Minerals. 2020;10:466. https://doi.org/10.3390/min10050466.

Publisher's Note